ORIGINAL PAPER

Finite-Element Simulation of a Resonant Frequency-Tunable Vibration Isolator Based on Shape Memory Alloy Wire

Jiefeng Li[1] · Xutao Nie[2] · Wei Zhang[2] · Yueyin Ma[2]

Abstract

Background The resonant-frequency-tunable vibration isolator based on Shape Memory Alloys (SMAs) combines the priority of passive and active vibration isolators, expands its engineering application, and improves the efficiency of vibration isolation. However, the special characteristics of SMAs and the complexity of the resonant-frequency-tunable vibration isolator result in the difficulty in finite-element analysis.

Methods This article employs the ABAQUS subroutine and presents the finite-element analysis for this resonant-frequency-tunable vibration isolator, which simulates the thermomechanical responses of SMA wires and the mechanical behaviors of the vibration isolator.

Results The pseudoelasticity characteristics of SMA wires were simulated and validated. The mechanical characteristics of the vibration isolator, such as the temperatures, martensitic volume fractions, displacements, and equivalent stresses, were obtained and verified.

Conclusions The results show that the finite-element analysis method presented is appropriate for simulating mechanical behaviors of the resonant-frequency-tunable vibration isolator. The analysis results reveal in detail the mechanical characteristics of the vibration isolator.

Keywords Finite-element simulation · Resonant-frequency-tunable · Vibration isolator · Shape memory alloy

Introduction

A vibration isolator is an effective way to attenuate structural vibration and protect the equipment and humans from harmful vibration to maintain precision and comfort [1, 2]. Conventional isolators are linear and passive [3], which keeps their characteristics unchanged throughout their entire service life and generally effectively suppresses low-frequency vibrations [4]. Isolators of this type have a limited range of application [5, 6], especially in the aerospace industry, where people and equipment are exposed to harmful vibrations with broadband spectra [7]. To expand the range of isolation, many approaches have been proposed, including

isolation systems with multiple degrees of freedom, variable-stiffness isolators, etc. In an effort to suppress vibration in three directions simultaneously, the Quasi-Zero stiffness multi-direction vibration isolation system has been developed, which includes symmetrically scissor-like structures in horizontal directions and a spring–mass–damper system in the vertical direction [8]. Ye et al. [9] designed an integrated translational–rotational vibration isolator with quasi-zero stiffness using a cam–roller mechanism that can provide high-static-low-dynamic stiffness in two directions simultaneously. Zhang et al. [10] devised a torsion-translational quasi-zero-stiffness isolator with a convex ball–roller mechanisms for attenuating torsion and translational vibrations along the shaft systems. Zhou et al. [11] constructed a quasi-zero stiffness vibration isolation platform with six degrees of freedom employing a new quasi-zero stiffness strut, which widens the vibration isolation band and has higher efficiency in a low-frequency range. Xu et al. [12] proposed a multi-directional Quasi-Zero-Stiffness vibration isolator with linear time-delayed active control. Their results

✉ Xutao Nie
  nie_xu_tao@163.com

1   Research Institute of Unmanned Aerial Vehicle, Nanjing University of Aeronautics and Astronautics, Nanjing 210016, China

2   China Aerodynamics Research and Development Center, Mianyang 621000, China

showed that the isolation efficiency of the isolator for different directions can be adjusted.

Melentjev et al. [13] studied an adjustable vibration isolator by changing the radius of curvature and the angle of coverage of the elastic element. The aim was to develop a method for calculating the load characteristics of controlled vibration isolators. Zhao et al. [14] proposed a bio-inspired semi-active vibration isolator with the dielectric elastomer based on a variable-stiffness element. The notable relative change in the stiffness of the elastomer could be achieved by increasing the pre-stretching and/or choosing the dielectric materials with the combination of a higher permittivity and a lower modulus of elasticity. Yan et al. [15] studied a nonlinear variable-stiffness vibration isolator with several axially asymmetric permanent magnets. Wu et al. [16] investigated systems with an adjustable stiffness by varying the effective spring length. Yan et al. [17] presented a bistable isolator with multiple ring permanent magnets and used nonlinear electromagnetic shunt damping. Analytical, numerical, and experimental efforts have shown that the proposed isolator could increase the isolation band and improve vibration isolation performance. Le et al. [18] developed a low-frequency vibration isolator that can adjust configurative parameters by a mechanism, offering a wide range of isolation, ensuring a load-bearing capacity and maintaining isolation efficiency.

However, all of the vibration isolators mentioned above are heavy, complicated and take up a lot of space, and all these adjustable approaches are implemented by mechanically changing the structures or shapes of the associated components. Recently, with the development of smart materials, such as shape memory alloys (SMAs), magnetorheological materials, etc., the resonant-frequency-tunable vibration isolators (RFTVIs) have been developed using smart materials whose stiffnesses can be actively adjusted [19–21]. In particular, SMAs exhibit different values of Young's modulus at high and low temperatures, which makes it possible to use them in RFTVIs. Meanwhile, the use of SMAs as elements of isolators has the advantages of compactness, lightness, high-energy density, and cost-effectiveness. However, only little literature was devoted to the use of SMAs as vibration elements [22, 23]. Shen et al. [23] introduced an RFTVI using SMA wires and metal rubber. This isolator can provide variable stiffnesses and tunable resonant frequencies. They focused on theoretical analysis and experimental verification. However, in practical engineering applications, experimental testing is complex, time-consuming, and costly, greatly delaying the design progress, which can be avoided by means of Finite Element Analysis (FEA). Due to the special characteristics of the nonlinear thermomechanical properties of SMAs, none of commercial FEA software packages available for SMAs can be applied to simulate their mechanical behaviors. Qidwai and Lagoudas [24] presented a numerical analysis that was based on

a unified thermomechanical constitutive model and used return mapping algorithms. Roh et al. [25] developed an incremental formulation of a 3D constitutive model to predict the thermomechanical characteristics of SMA strips, in which the finite-element program coded with FORTRAN was used to simulate the SMA strips.

In this paper, the unified SMA constitutive model presented by Lagoudas et al. [26] was adopted to simulate the responses of SMA wires in the RFTVI, and the basic theoretical formulas were presented. Then, the mechanical characteristics of the main components of the isolator were analyzed in detail, which revealed the mechanical behaviors of these components.

The paper is organized as follows. "Introduction of the RFTVI with SMA wires" section briefly introduces the design and philosophy of the RFTVI. "Material subroutine principle for SMA" section presents the unified SMA constitutive model, an inverse mapping algorithm, and consistent tangent stiffness moduli. In "Demonstration of UMAT Subroutine for SMAs" section, the parameters contained in the basic model are determined, and the UMAT (user-defined material mechanical behavior) subroutine for SMA wires is implemented and verified. In "Simulating the mechanical behavior of the RFTVI" section, the finite-element model of the RFTVI is established in ABAQUS, a key connector among the components is set, and the analysis steps are defined. In "Experimental verification of the RFTVI" section, the vibration experiments were carried out to demonstrate the isolation performance of the RFTVI. The simulation and experimental results are given and discussed in "Results and Discussion" section. Finally, some conclusions are summarized in "Summary and Conclusion" section.

Introduction of the RFTVI with SMA Wires

Structure of the RFTVI

The structure of the RFTVI is shown in Fig. 1. Figure 1a, b is the isometric view and sectional view, respectively. The components of the RFTVI include one base support, one inner support, one spring, two annular metal rubbers, one upper plate, one movable spindle, six SMA wires, twelve SMA wires fixers, and three guide bolts. The materials of these components consist of four types: Ni (49.4 wt.%)-Ti (50.6 wt.%) alloy wire with 1 mm diameter for SMA wires, 0Cr18Ni9 alloy wire with 0.15 mm diameter for annular metal rubbers, 60Si2Mn alloy wire with 2 mm diameter for spring, and 30CrMnSi for other components. The properties of 30CrMnSi are listed in Table 1. The stiffness coefficient of the 60Si2Mn spring is 36 N/mm. The properties of the metal rubbers were determined by the following test. The

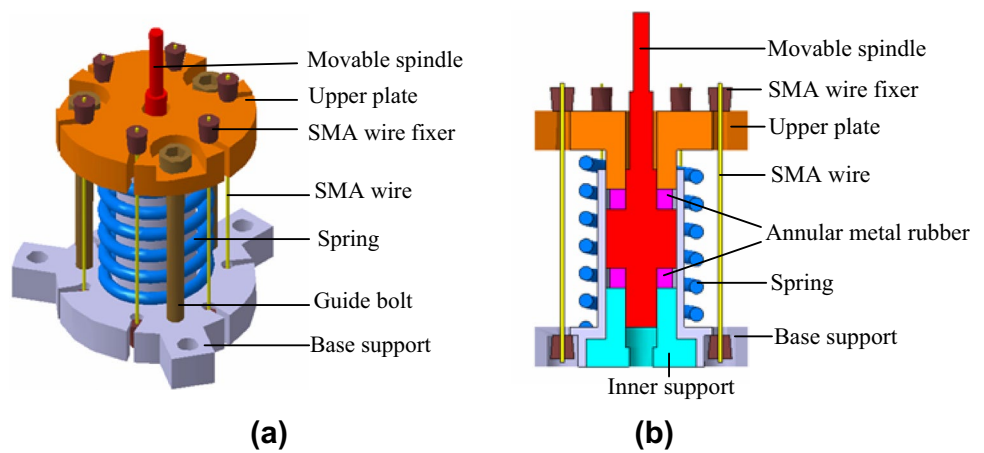Fig. 1 Structure of the RFTVI: **a** isometric view; **b** sectional view

Table 1 Materials properties of alloy 30 CrMnSi

Material type	Density, ρ	Poisson's ratio, υ	Young's modulus, E	Tensile strength, σ_b
30CrMnSi	7.85 g/cm^3	0.3	210 GPa	980 MPa

special mechanical characteristics of SMA wire will be discussed in Sect. 3.

The assembly sequence of the RFTVI is from the bottom to the top and from the inside to the outside. The assembly process is described as follows: First, the inner support was inserted into the base support through the central hole. Second, one metal rubber was placed on the top surface of the inner support. Third, the thicker end of the movable spindle was put in the central hole of the assembled metal rubber. Fourth, another metal rubber was placed on the platform of the movable spindle. Fifth, the spring was sleeved on the outer cylinder of the base support. Sixth, the upper plate was laid over the upper metal rubber. Seventh, the guide bolts were assembled between the base support and upper plate and tightened to compress the spring to produce a displacement of 0.4 mm in Z-axis direction. Finally, six pre-strained

SMA wires were fastened between the base support and the upper plate with fixers.

The Principle of an RFT Vibration Isolator

This RFTVI can perform two resonant frequencies, low resonant frequency and high resonant frequency, by tuning the state of SMA wires. At a low resonant frequency, pre-strained SMA wires are in a martensitic state with a low Young's modulus. Whereas a high resonant frequency is achieved by heating the SMA wire, which can activate the transformation from martensite into austenite with a high Young's modulus. Due to the phase transformation, the SMA wires shrink and compress the annular metal rubbers and spring, which results in the generation of internal stress in the metal rubbers and spring. Then, the stiffness of the metal rubbers is improved. Stop heating, the SMA wires will transform from austenite with high Young's modulus into martensite with a low Young's modulus, so that the spring can resist the strain of SMA wires and metal rubbers. Consequently, the resonant frequency of the RFTVI returns to the original low resonant frequency.

Fig. 2 Photos of **a** metal rubber and **b** test fixtures
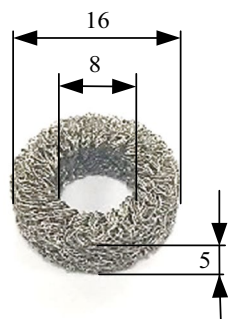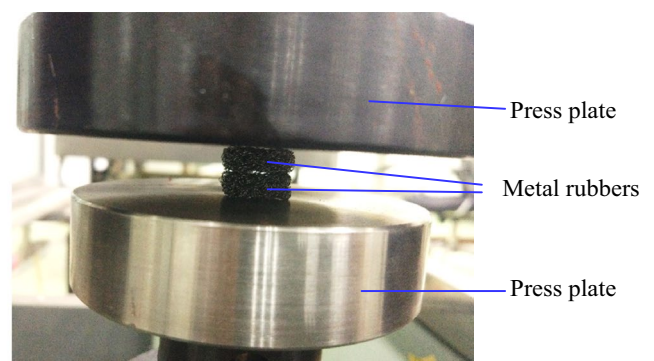
Determination of the Mechanical Properties of Annular Metal Rubbers

Annular metal rubbers assembled in the vibration isolator are made of 0Cr18Ni9 stainless steel wire with a density 7.93 g/cm^3. Figure 2a is the photo of a metal rubber. The dimensions of a metal rubber, including the outer diameter, inner diameter, and height, are 16, 8, and 5 mm, respectively. Because the mechanical properties of annular metal rubber depend on their relative density ratio and the wire diameter, the properties of metal rubbers should be determined experimentally. In this work, the relative density ratio of the metal rubber is 20%, which is calculated by the following expression:

$$\rho_r = \frac{\pi r_0^2 l \rho}{\pi (R^2 - r^2) h \rho}, \tag{1}$$

where ρ_r is the relative density ratio; r_0, l, and ρ are the diameter, length, and density of stainless steel wire, respectively; R, r, and h are the outer diameter, inner diameter, and height of the metal rubber.

To obtain the mechanical parameters of a metal rubber, quasi-static compression tests were carried out with a universal testing machine UTM13307. Corresponding to the practical state in the vibration isolator, two metal rubbers stacked together were tested at the same time. In addition, two press plates were employed to uniformly distribute the compressive load on the metal rubbers. Figure 2b shows the test fixtures. During the test, first, a displacement of 0.103 mm was applied to the metal rubbers to ensure that their surfaces were in sufficient contact with the press plates. Second, the two metal rubbers were pressed at the rate

1.67×10^{-2} mm/s until the displacement was 1 mm. Finally, the pressure was released at the same velocity. During the loading–unloading process, the data of forces and displacements were recorded. Based on the experimental data, a force–displacement curve for two metal rubbers was plotted, as shown in Fig. 3. As can be seen. With the forces increasing, the displacements increase nonlinearly in the loading process, while the displacements decrease almost linearly with force decreasing in the unloading process. In addition, there is a hysteresis loop between the loading and unloading curves, which represents the dissipative energy.

Material Subroutine Principle for SMA

SMA Constitutive Model

The unified SMA constitutive model proposed by Lagoudas et al. was developed through constructing the Gibbs free energy function of a volume element, which was constrained by the second law of thermodynamics [24, 26]. Meanwhile, the yield surface of SMA phase transformation was defined. This unified constitutive model is briefly presented here. Gibbs free energy is chosen as the thermodynamic potential, which contains a thermoelastic part and a nonlinear transformation strengthens part. First, the transformation strain tensor $\boldsymbol{\varepsilon}^t$ and the volume fraction martensitic ξ were chosen as internal state variables. Then the Gibbs free energy has the following form:

$$\begin{aligned} G(\sigma, T, \xi, \varepsilon^t) = &-\frac{1}{2\rho}\sigma : S : \sigma - \frac{1}{\rho}\sigma : [\alpha(T - T_0) + \varepsilon^t] \\ &+ c\left[(T - T_0) - T\ln\left(\frac{T}{T_0}\right)\right] - s_0 T + u_0 + \frac{1}{\rho}f(\xi), \end{aligned} \tag{2}$$

where $\boldsymbol{\sigma}$ is the Cauchy stress tensor, $\boldsymbol{\varepsilon}^t$ is the transformation strain tensor, ξ is the martensitic volume fraction, T is the current temperature, T_0 is the reference temperature. S, $\boldsymbol{\alpha}$, ρ, c, s_0, u_0 are the effective compliance tensor, the effective expansion tensor, the density, the effective specific heat, the effective entropy at reference state and the effective specific internal energy at reference state, respectively. The function $f(\xi)$ is a transformation hardening function. The above material parameters correspond to the mixing rule, which can be written as

$$S = S^A + \xi(S^M - S^A) = S^A + \xi \Delta S \tag{2.1}$$

$$\alpha = \alpha^A + \xi(\alpha^M - \alpha^A) = \alpha^A + \xi \Delta \alpha \tag{2.2}$$

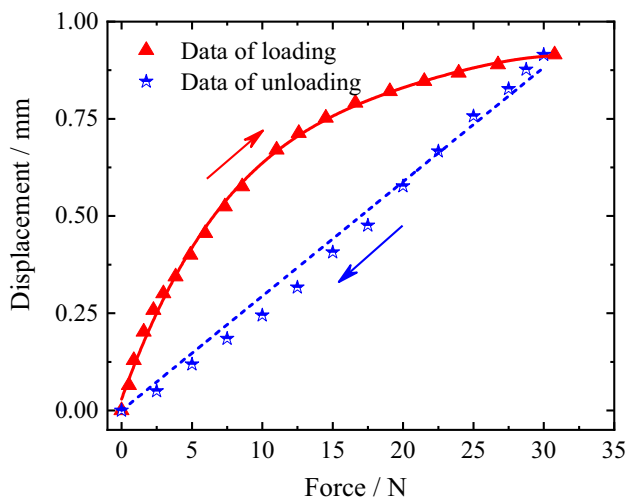$$c = c^A + \xi(c^M - c^A) = c^A + \xi \Delta c \tag{2.3}$$

Fig. 3 Displacement–force curve for two metal rubbers

$$s_0 = s_0^A + \xi(s_0^M - s_0^A) = s_0^A + \xi\Delta s_0 \tag{2.4}$$

$$u_0 = u_0^A + \xi(u_0^M - u_0^A) = u_0^A + \xi\Delta u_0, \tag{2.5}$$

where the superscripts M and A denote the martensitic phase and austenitic phase respectively. The prefix Δ indicates the difference in the amount of austenite and martensite. The relation between Gibbs free energy and internal energy can be obtained using the Legendre transformation as follows:

$$G(\sigma, T, \xi, \varepsilon^t) = u - \frac{1}{\rho}\sigma : \varepsilon - sT, \tag{3}$$

where the sign (:) represents the double dot product operation between the two tensors σ and ε. Substituting the Eq. (3) for the Gibbs free energy and the internal energy into the first law and the second law of thermodynamics, expressed in the Clausius–Planck inequality, the following expression is obtained:

$$-\rho\dot{G} - \dot{\sigma} : \varepsilon - \rho s\dot{T} \geq 0, \tag{4}$$

where the sign (˙) indicates the material time derivative operation. Using the method of fixing all but one variable, the constitutive relation can be obtained

$$\varepsilon = -\rho\frac{\partial G}{\partial\sigma} = S : \sigma + \alpha(T - T_0) + \varepsilon^t. \tag{5}$$

Formulation Eq. 5 indicates that total strain consists of elastic strain, thermal expansion strain, and phase transformation strain. In this model, the martensitic volume fraction ξ and transformation strain ε^t are internal state variables, which have the following relation:

$$\dot{\varepsilon}^t = \Lambda\dot{\xi}, \tag{6}$$

where the Λ is the transformation tensor, which defines the direction of the transformation and has the following form:

$$\Lambda = \begin{cases} \frac{3}{2}H\frac{\sigma'}{\bar{\sigma}'}, & \dot{\xi} > 0 \\ H\frac{\varepsilon^{t-r}}{\bar{\varepsilon}^{t-r}}, & \dot{\xi} < 0 \end{cases} \tag{7}$$

where H is the maximum transformation strain under uniaxial loading and σ' is the deviatoric stress tensor defined by the formula

$$\sigma' = \sigma - \frac{1}{3}\text{tr}(\sigma)1. \tag{8}$$

σ' is the effective stress, which can be written as

$$\bar{\sigma}' = \sqrt{\frac{3}{2}\|\sigma'\|^2}. \tag{9}$$

Furthermore, ε^{t-r} is the transformation strain and $\bar{\varepsilon}^{t-r}$ is the effective transformation strain at the point of reverse

transformation (austenite to martensite). The relation between ε^{t-r} and $\bar{\varepsilon}^{t-r}$ has the following form:

$$\bar{\varepsilon}^{t-r} = \sqrt{\frac{2}{3}\|\varepsilon^{t-r}\|^2}. \tag{10}$$

The thermodynamic force π can be obtained by combining the Eqs. (3), (4), (5), and (6), which is written as

$$c\pi(\sigma, T, \xi) = \sigma : \Lambda + \frac{1}{2}\sigma : \Delta S : \sigma + \sigma : \Delta\alpha(T - T_0)$$
$$- \rho\Delta c\left[(T - T_0) - T\ln\left(\frac{T}{T_0}\right)\right] + \rho\Delta s_0 T - \frac{\partial f}{\partial\xi} - \rho\Delta u_0. \tag{11}$$

To capture the forward and reverse martensitic transformation, a transformation function Φ is introduced, such that

$$\Phi = \begin{cases} \pi - Y, & \dot{\xi} > 0 \quad (A \to M) \\ -\pi - Y, & \dot{\xi} < 0 \quad (M \to A) \end{cases} \tag{12}$$

Note that Y is a material constant that is a measure of internal dissipation due to phase transformation. In addition, the constraints on the martensitic volume fraction are introduced for both forward and reverse phase transformations

$$\dot{\xi} \geq 0; \quad \Phi(\sigma, T, \xi) \leq 0; \quad \Phi\dot{\xi} = 0 \tag{13}$$

$$\dot{\xi} \leq 0; \quad \Phi(\sigma, T, \xi) \leq 0; \quad \Phi\dot{\xi} = 0. \tag{14}$$

For constitutive model presented by Boyd and Lagoudas [24], the transformation hardening function $f(\xi)$ takes the following form:

$$f(\xi) = \begin{cases} \frac{1}{2}\rho b^M\xi^2 + (\mu_1^p + \mu_2^p)\xi, & \dot{\xi} > 0, \\ \frac{1}{2}\rho b^A\xi^2 + (\mu_1^p - \mu_2^p)\xi, & \dot{\xi} < 0. \end{cases} \tag{15}$$

The quantities b^M, b^A, μ_1, and μ_2 are material constants that can be determined experimentally or from micromechanics evaluations.

Tangent Moduli Tensor of Continuum

The increments of the constitutive model can be written as the form of increment of the stress tensor

$$d\sigma = \Gamma : d\varepsilon + \Theta dT, \tag{16}$$

where Γ is the tangent stiffness tensor and Θ is the tangent thermal moduli tensor. By means of the differential form of the transformation function and constitutive relation (5), the relationship between the stress, strain and temperature is obtained as

$$d\sigma = \left[S^{-1} - \frac{S^{-1}:\partial_\sigma\Phi\otimes S^{-1}:\partial_\sigma\Phi}{\partial_\sigma\Phi:S^{-1}:\partial_\sigma\Phi - \partial_\xi\Phi}\right] : d\varepsilon + S^{-1} : \left[\partial_\sigma\Phi\left(\frac{\partial_\sigma\Phi:S^{-1}:\alpha - \partial_T\Phi}{\partial_\sigma\Phi:S^{-1}:\partial_\sigma\Phi - \partial_\xi\Phi}\right) - \alpha\right]dT. \tag{17}$$

Then, the tangent stiffness tensor and the tangent thermal moduli tensor are obtained as follows:

$$\Gamma = S^{-1} - \frac{S^{-1} : \partial_\sigma \Phi \otimes S^{-1} \partial_\sigma \Phi}{\partial_\sigma \Phi : S^{-1} : \partial_\sigma \Phi \pm \partial_\xi \Phi} \tag{18}$$

$$\Theta = -\Gamma : \alpha - \partial_T \Phi \frac{S^{-1} : \partial_\sigma \Phi}{\partial_\sigma \Phi : S^{-1} : \partial_\sigma \Phi \pm \partial_\xi \Phi}, \tag{19}$$

where the sign "$\pm$" represents the forward (austenite to martensite) or reverse (martensite to austenite) phase transformation, respectively.

Finite-Element Analysis Algorithms for the SMA Constitutive Model

Based on the above SMA constitutive model, return mapping algorithms are used to calculate the stress increment. A User Material Subroutine (UMAT) of SMA is then programmed, which numerically simulates the mechanical behavior of SMA. Nonlinear thermomechanical prediction of transformation evolution can be divided into a thermoelastic prediction problem and a transformation correction problem in accordance with the constitutive relation.

First, the thermoelastic prediction is considered. It is assumed that the increment of the martensitic fraction is zero, i.e., $\Delta \xi = 0$. Considering the time interval $[0, t]$, $t_n \in [0, t]$, $t_{n+1} \in [0, t]$ and $t_{n+1} > t_n$, the thermoelastic prediction can be expressed in the following form:

$$\varepsilon_{n+1} = \varepsilon_n + \Delta \varepsilon_{n+1} \tag{20.1}$$

$$T_{n+1} = T_n + \Delta T_{n+1} \tag{20.2}$$

$$\varepsilon_{n+1}^{tr}{}^{(0)} = \varepsilon_n^{tr} \tag{20.3}$$

$$\xi_{n+1}^{(0)} = \xi_n \tag{20.4}$$

$$\sigma_{n+1}^{(0)} = S_n^{-1} : \left[\varepsilon_{n+1} - \alpha_n \left(T_{n+1} - T_0 \right) - \varepsilon_n^t \right] \tag{21}$$

$$\Phi_{n+1}^{(0)} = \Phi \left(\sigma_{n+1}^{(0)}, T_{n+1}, \xi_n \right), \tag{22}$$

where $\Delta \varepsilon_{n+1}$, ΔT_{n+1} are the strain tensor and temperature increments, respectively, over the time step $[t_n, t_{n+1}]$. The superscript "(0)" represents the values obtained in the prediction stage.

Second, the transformation correction is analyzed. The increment of strain tensor is given by

$$c\Delta \varepsilon_{n+1} = \Delta S_{n+1} : \sigma_{n+1} + S_{n+1} : \Delta \sigma_{n+1} + \Delta \alpha_{n+1} \left(T_{n+1} - T_0 \right) + \alpha_{n+1} \Delta T_{n+1} + \Delta \varepsilon_{n+1}^t, \tag{23}$$

where the increment of the compliance tensor is expressed as $\Delta S_{n+1} = \Delta \xi_{n+1} \Delta S$. The increment of the thermal expansion coefficient is $\Delta \alpha_{n+1} = \Delta \xi_{n+1} \Delta \alpha$. Then, the increment of the stress tensor for kth iteration is calculated as follows:

$$\Delta \sigma_{n+1}^{(k)} = -\Delta \xi_{n+1}^{(k)} \Delta S_{n+1}^{(k)^{-1}} : \begin{cases} \partial_\sigma \Phi_{n+1}^{(k)} & \dot{\xi} > 0 \\ -\partial_\sigma \Phi_{n+1}^{(k)} & \dot{\xi} < 0 \end{cases}. \tag{24}$$

The derivative of the transformation function with respect to the stress tensor is given by

$$\partial_\sigma \Phi_{n+1}^{(k)} = \begin{cases} \Delta S : \sigma_{n+1}^{(k)} + \Delta \alpha \left(T_{n+1} - T_0 \right) + \Lambda_{n+1}^{(k)} & \dot{\xi} > 0 \\ -\Delta S : \sigma_{n+1}^{(k)} - \Delta \alpha \left(T_{n+1} - T_0 \right) - \Lambda_{n+1}^{(k)} & \dot{\xi} < 0 \end{cases}. \tag{25}$$

By linearizing the transformation function, the following consistency condition is obtained as:

$$\Phi_{n+1}^{(k)} + \partial_\sigma \Phi_{n+1}^{(k)} : \Delta \sigma_{n+1}^{(k)} + \partial_\xi \Phi_{n+1}^{(k)} : \Delta \xi_{n+1}^{(k)} = 0. \tag{26}$$

Using the above equations, we can derive the increment of martensitic volume fraction for kth iteration

$$\Delta \xi_{n+1}^{(k)} = \frac{\Phi_{n+1}^{(k)}}{\pm \partial_\sigma \Phi_{n+1}^{(k)} : S_{n+1}^{(k)} : \partial \Phi_{n+1}^{(k)} - \partial_\xi \Phi_{n+1}^{(k)}}, \tag{27}$$

where the sign "$\pm$" denotes the forward and reverse transformations, respectively. The transformation function is then used to update the transformation strain and martensitic fraction for $(k + 1)$th iteration.

Demonstration of UMAT Subroutine for SMAs

Determination of Material Parameters

The material parameters required for the UMAT subroutine include direct and indirect parameters. The direct parameters can be tested experimentally, while indirect parameters need to be calculated from direct parameters. Direct parameters include martensite start and finish temperatures and austenite start and finish temperatures at zero stress M_s, M_f, A_s, A_f, Young's moduli of martensite and austenite E_M, E_A, the maximum transformation strain H, initiation and completion stresses of martensitic transformation σ^{M_s}, σ^{M_f}, initiation and

completion stresses of austenitic transformation σ^{A_s}, σ^{A_f}. The indirect parameters include stress influence coefficient$\rho\Delta s_0$, thermal expansion coefficients of martensite and austeniteα_M,α_A. The methods for determination of these parameters are briefly described below.

The four transformation temperatures M_s,M_f,A_s, A_f were determined from a Differential Scanning Calorimeter test. The Young's moduli E_M,E_A, the maximum transformation strain and four critical transformation stresses σ^{M_s},σ^{M_f}, σ^{A_s}, σ^{A_f} were obtained from a uniaxial pseudoelastic test. The stress influence coefficient $\rho\Delta s_0$ was calculated from transformation function in one-dimensional model. The thermal expansion coefficientsα_M, α_A were determined from the slopes of the strain–temperature plot in the fully martensitic and austenitic states, respectively.

The material parameters of the SMA wire used in this paper are listed in Table 2.

Numerical Simulation for SMA Wire Based on the UMAT Subroutine

According to the numerical algorithms for the SMA constitutive model, the UMAT subroutine was coded in FORTRAN. Then a finite-element model of the SMA wire was created to simulate its pseudoelasticity. The analysis results were compared with the experimental results.

The finite-element model of SMA wire is shown in Fig. 4. The elements used in this model are 3D 20-node solid elements C3D20R. The material parameters adopted in the simulation are taken from Table 1. The SMA wire has a diameter of 1 mm and a length of 50 mm. One end of the SMA wire is fixed and the other end is loaded with an axial tensile force P. Initially, the SMA wire is in the fully austenitic state
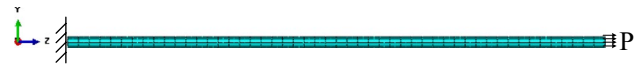
Fig. 4 Finite-element model of SMA wire

and at a temperature of 343 K higher than A_f. The loading cases include loading and unloading. First, an axial tensile force, from zero to maximum stress of 550MP, was applied on the SMA wire. During this procedure, the martensitic transformation took place until the fully martensitic sate was achieved. Meanwhile, the maximum transformation strain H was obtained. Then, the tensile force was released to zero, which resulted in the recovery of the transformation strain. The same analysis was conducted at a temperature of 348 K. To verify the simulations, uniaxial tensile tests were performed correspondingly. The experimental results were compared with simulation results, as shown in Fig. 5.

Figure 5a, b is the stress vs. strain curve obtained at temperatures of 343 and 348 K, respectively. As can be seen, the stress–strain curves of simulations are consistent with the experimental results, either at a temperature of 343 K or 348 K, which exhibit the mechanical characteristics of pseudoelasticity of SMA wire. In addition, the four critical transformation stresses can be obtained from the curves. At the temperature of 343 K, the values of σ^{M_s}, σ^{M_f}, σ^{A_s}, and σ^{A_f} are 336, 415, 148, and 63 MPa, respectively, while at the temperature of 348 K, are 371, 438, 194, and 106 MPa, respectively.

The detailed simulation results at the temperature of 343 K are shown in Figs. 6, 7, 8, 9. Figure 6a, b shows the stress and martensitic volume fraction distribution, respectively, at the beginning of the forward transformation. It

| No	Material parameters	Value
1	Martensite start temperature M_s	302 K
2	Martensite finish temperature M_f	291 K
3	Austenite start temperature A_s	326 K
4	Austenitic finish temperature A_f	336 K
5	Young's martensitic modulus E_M	2×10^4 MPa
6	Young's austenitic modulus E_A	4×10^4 MPa
7	Poisson's ratio (equal for both phase) υ	0.33
8	Coefficient of thermal expansion for the martensite α_M	2.2×10^{-5}
9	Coefficient of thermal expansion for the austenite α_A	2.2×10^{-5}
10	Maximum transformation strain H	0.034
11	Stress influence coefficient (equal for both phase) $\rho\Delta s_0$	–0.3131
12	Stress for initiation of martensitic transformation (at 343 K) σ^{M_s}	336 MPa
13	Stress for completion of martensitic transformation (at 343 K) σ^{M_f}	415 MPa
14	Stress for initiation of austenitic transformation (at 343 K) σ^{A_s}	148 MPa
15	Stress for completion of austenitic transformation (at 343 K) σ^{A_f}	63 MPa

Table 2 Material parameters for SMA wire
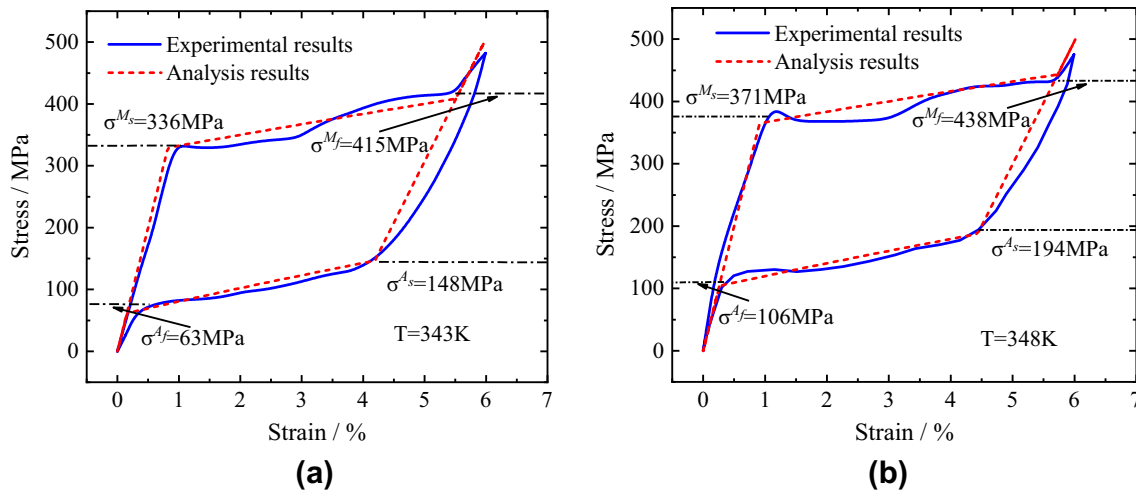
Fig. 5 Stress–strain curves of SMA wires obtained at **a** 343 K and **b** 348 K
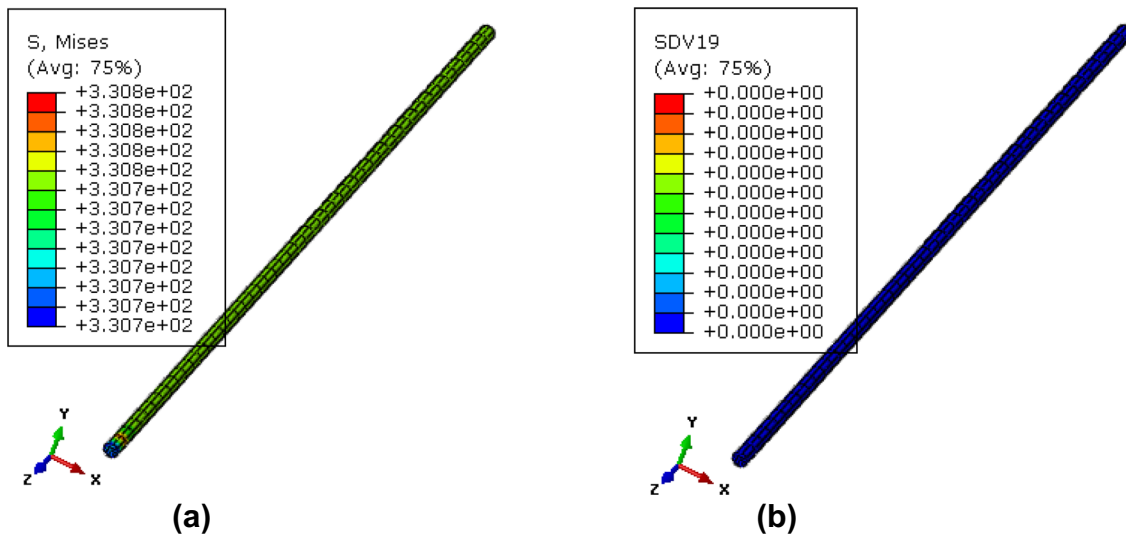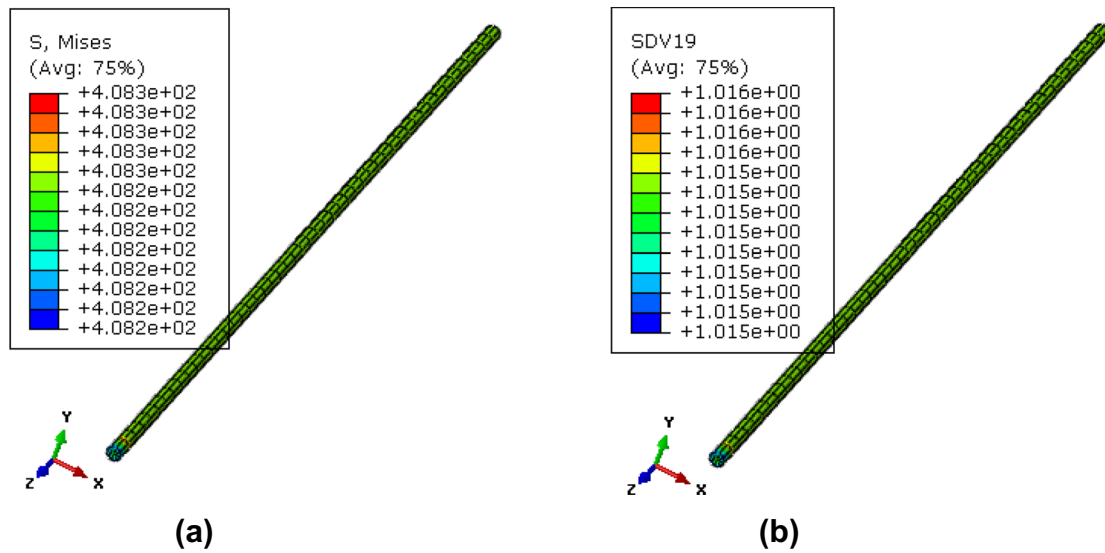

Fig. 6 Results of **a** stress distribution and **b** Martensitic volume fraction distribution obtained at the beginning of the forward transformation at 343 K

is seen that the distributions of stress and the martensitic volume fraction are uniform. In addition, the value of the martensitic volume fraction is zero, which is in good agreement with the theoretical value. The stress is 331 MPa, which has a relative error of 1.49% in comparison with the experimental result of 336 MPa.

Figure 7a, b shows the stress and martensitic volume fraction distribution, respectively, at the end of the forward transformation. As can be seen, the stress and the martensitic volume fraction distribution are approximately uniform with a value of 408.3 MPa and 1.02, respectively. The relative error of stress is 1.61% compared to the experimental result of 315 MPa, while the relative error

of martensitic volume fraction is 2.0% compared to the exact solution of 1.

Figure 8a, b shows the stress and martensitic volume fraction distribution, respectively, at the beginning of the reverse transformation. As can be seen from these figures, the stress value is approximately 146.8 MPa, which has a relative error 0.81% compared to the experimental result of 148 MPa. The martensitic volume fraction is 1.016 with a relative error of 1.6% compared to the exact solution of 1.

Figure 9a, b shows the stress and martensitic volume fraction distribution, respectively, at the end of the reverse transformation. It can be seen that the stress value is 61.7 MPa

Fig. 7 Results of **a** stress distribution and **b** Martensitic volume fraction distribution obtained at the end of the forward transformation at 343 K
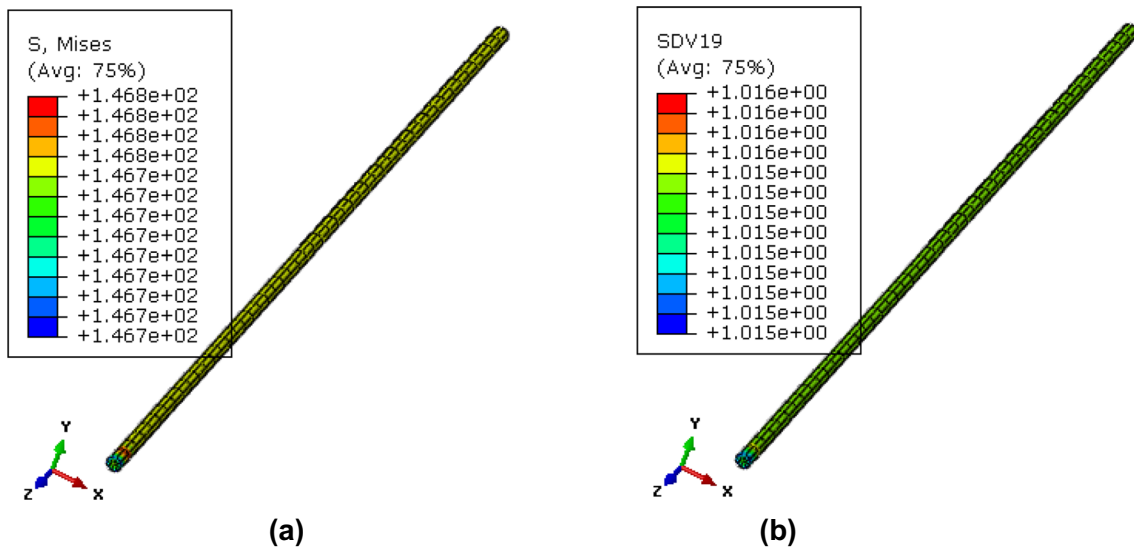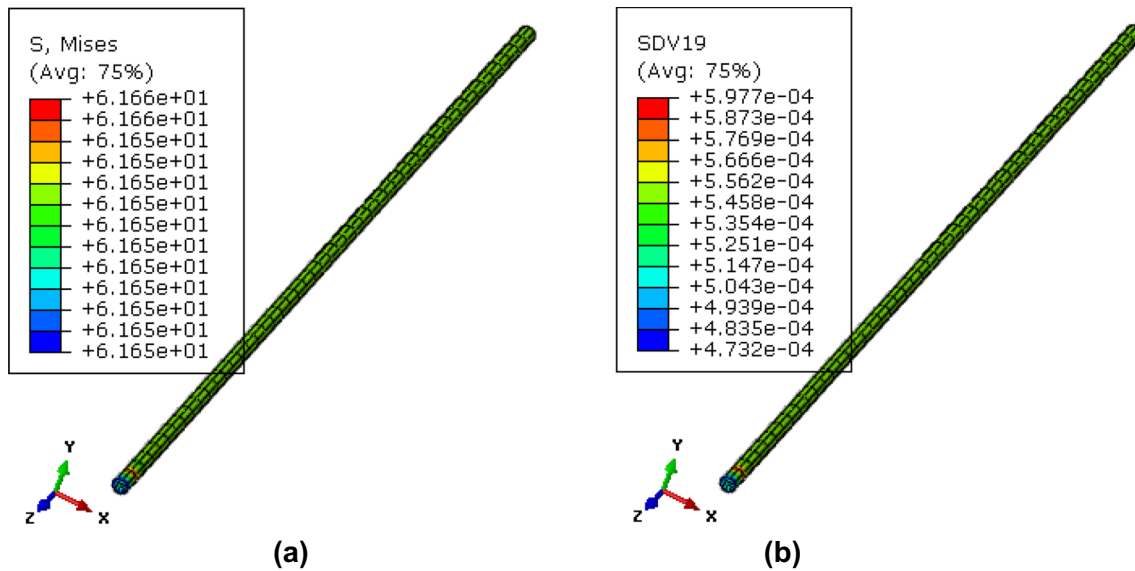

Fig. 8 Results of **a** stress distribution and **b** Martensitic volume fraction distribution obtained at the beginning of the reverse transformation at 343 K
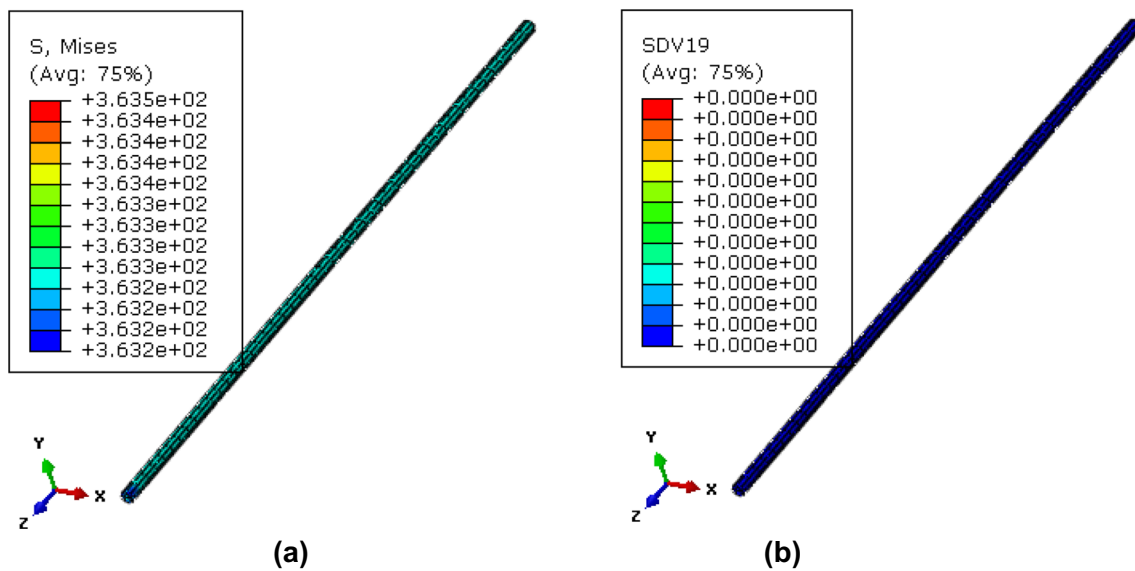
with a relative error of 2.06% compared to the experimental result of 63 MPa, while the martensitic volume fraction is 5×10^{-4} with a relative error of 0.05% compared to the exact solution of zero.

Figures 10, 11, 12, 13 show the simulation results at a temperature of 348 K. Figure 10a, b shows the stress and martensitic volume fraction distribution, respectively, at the beginning of the forward transformation. It is seen that the stress value is approximately equal to 363 MPa, and the martensitic fraction is zero. The relative error of stress is 2.16% compared to the experimental result of 371 MPa, while the martensitic fraction is equal to exact solution.

Figure 11a, b shows the stress and martensitic volume fraction distribution, respectively, at the end of the forward transformation. It can be seen that the stress value is approximately 443 MPa, and the martensitic fraction is 1.02. The relative error of stress is 1.14% compared to the experimental result of 438 MPa, while the relative error of martensitic volume fraction is 2% compared to the accurate solution of 1.

Figure 12a, b shows the stress and martensitic volume fraction distribution, respectively, at the beginning of the reverse transformatioin. These results show that the stress value is approximately 189 MPa, and the martensitic volume
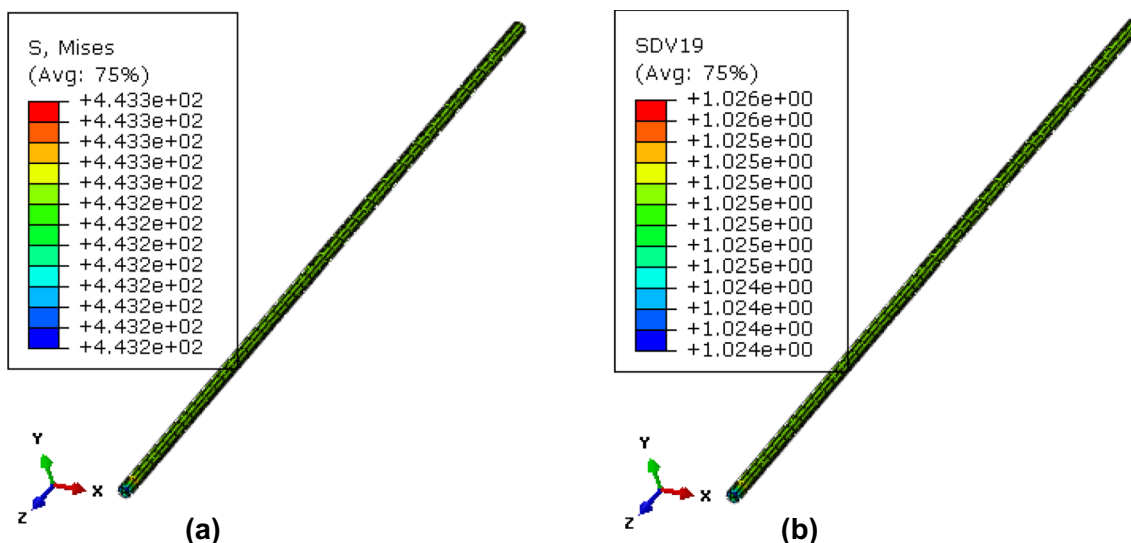
Fig. 9 Results of **a** stress distribution and **b** Martensitic volume fraction distribution obtained at the end of the reverse transformation at 343 K

Fig. 10 Results of **a** stress distribution and **b** Martensitic volume fraction distribution obtained at the beginning of the forward transformation at 348 K

fraction is 1.025. The relative error of stress is 2.58% compared to the experimental result of 194 MPa, while the relative error of martensitic volume fraction is 2.5% compared to the accurate solution of 1.

Figure 13a, b shows the stress and martensitic volume fraction distribution, respectively, at the end of the reverse transformatioin. It can be seen that the stress value is 104 MPa with a relative error of 1.89% compared to the experimental result 106 MPa, while the martensitic volume fraction is approximately 8×10^{-4} with a relative error of 0.08% compared to the exact solution of zero.

The above results show that the simulation accuracy can meet the application of SMA wires in engineering. The finite-element analysis method adopted is valid in simulating the mechanical behavior of SMA wires.

Fig. 11 Results of **a** stress distribution and **b** Martensitic volume fraction distribution obtained at the end of the forward transformation at 348 K
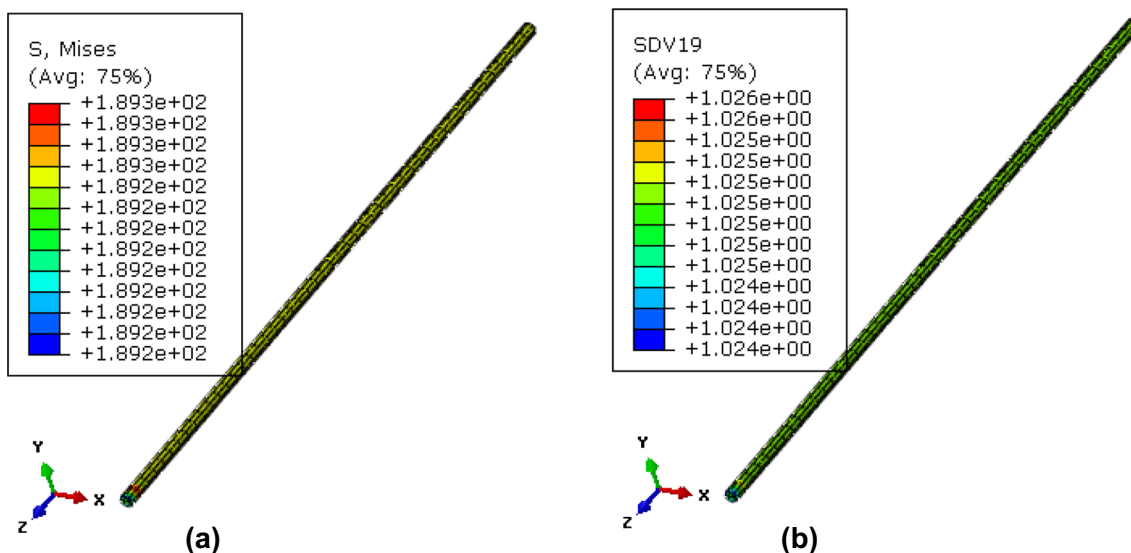
Fig. 12 Results of **a** stress distribution and **b** Martensitic volume fraction distribution obtained at the beginning of the reverse transformation at 348 K

Simulating the Mechanical Behavior of the RFTVI

Model of the RFTVI

The thermomechanical behavior of an RFTVI is simulated in ABAQUS environment, and its three-dimensional finite-element model is shown in Fig. 14a. To simplify the simulation, the inner support and the base support are considered as a whole component. Figure 14b shows the TRANSLATOR CONNECTOR and SPRING elements. Here, the TRANSLATOR CONNECTOR elements were employed to simulate the two metal rubbers, which were constructed between the base support and the movable spindle and between the upper plate and the movable spindle. The mechanical properties of the TRANSLATOR CONNECTOR element are given by the test data of metal rubbers. The SPRING element was employed to simulate the spring between the upper plate and the base support with an elastic stiffness of 36 N/mm. The properties of SMA wires were defined by the UMAT subroutine, where the initial martensitic fraction and the initial transformation strain are 0.6 and 0.02, respectively, in accordance with the experiments.
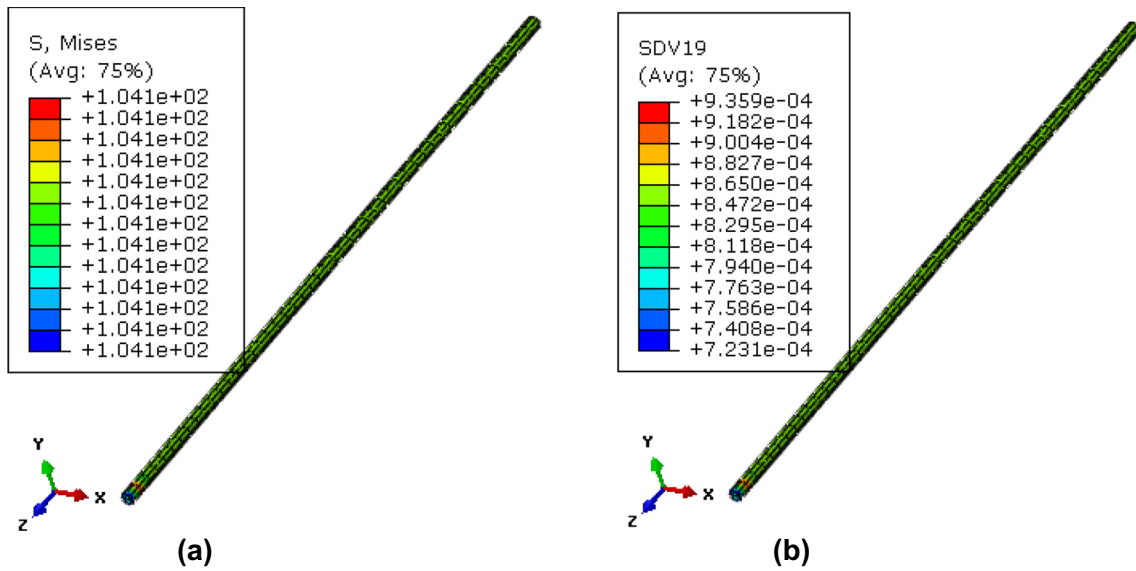
Fig. 13 Results of **a** stress distribution and **b** Martensitic volume fraction distribution obtained at the end of the reverse transformation at 348 K
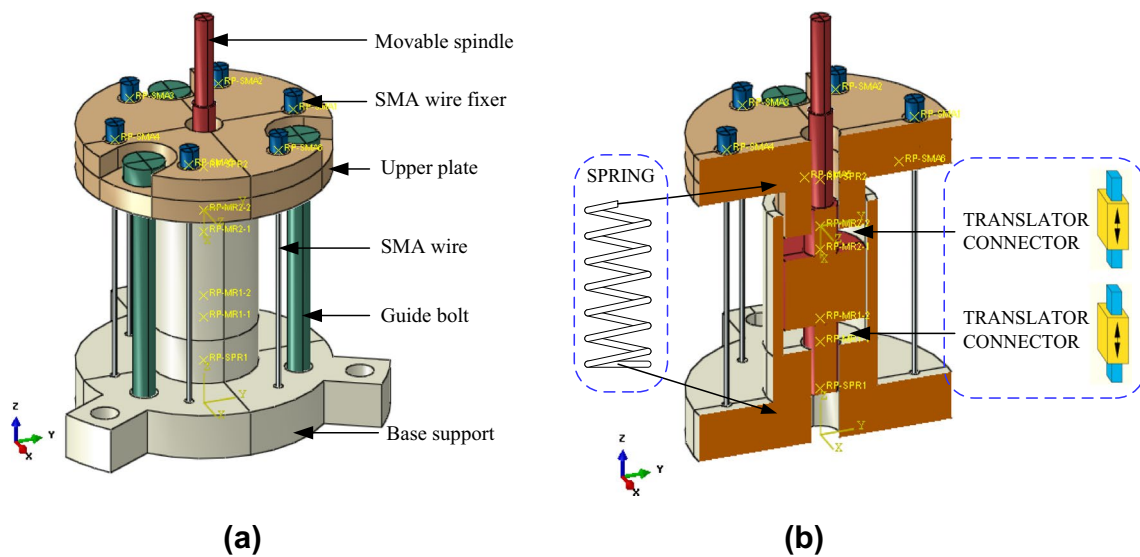

Fig. 14 **a** Three-dimensional model of the FRTVI and its components. **b** TRANSLATOR CONNECTOR and SPRING elements

Load Steps for Mechanical Simulation

Two load steps are defined to simulate the assembly and working procedures of the RFTVI, respectively. The first load step is a mechanical load, which is applied on the guide bolts and induces a compressive displacement of 0.4 mm in the z-axis direction of the guide bolts. Thus, the upper plate is driven to compress each metal rubber to produce a displacement of 0.2 mm. Meanwhile, a pressure is gradually applied on the lower surface of the upper plate to simulate the reaction force of the spring until the maximum value of 0.82 MPa is reached.

The second step is a thermal load, which is applied on the SMA wires to simulate their activating process. During this process, the SMA wires are thermally insulated from their adjacent parts, and their temperatures were raised from 280 to 400 K. With the increase of temperature, the SMA wires transform from the martensitic sate into austenitic sate, which induces the contraction of SMA wires. Thus, the spring and two metal rubbers are further compressed, and the structural stiffness of the RFT vibration isolator is increased.

Experimental Verification of the RFTVI

The isolation performance of the RTFVI is evaluated by the force transmissibility T, which is defined as the ratio of the response amplitude to the base excitation amplitude. Since the base excitation and response have the identical angular velocities, the force transmissibility is also equal to the ratio of their acceleration amplitudes. Under the condition of simple harmonic excitation, the vibration transmissibility is equal to the acceleration ratio, as follows:

$$T = T_a = \frac{B_d}{\bar{v}} = \frac{a_{out}}{a_{in}} \tag{28}$$

where T_a is the acceleration transmissibility, B_d is the response amplitude, $\bar{v}$ is the base excitation amplitude, a_{out} is the response acceleration, and a_{in} is the base excitation acceleration.

The experimental platform were set up to verify the vibration isolator performance of the RFTVI. Figure 15 shows the schematic of the experimental setup. A shaking table was adopted as vibration source. A 1 kg mass was installed on the top of the RFTVI. Acceleration sensor 1 placed on the shaking table and sensor 2 placed on the mass were employed to acquire the acceleration of the shaking table and mass, respectively. The vibration controller was used to receive the data from the two acceleration sensors and transmitted the data to the computer after processing. The power amplifier amplified the control signal and input it to the shaking table. A DC power supply was applied to activate the SMA wires through Joule heat, so as to tune the resonant frequency of the RFTVI. During the test, a sinusoidal sweep test ranging from 5 to 500 Hz was implemented by the shaking table. The acceleration a_{in} and a_{out} were gathered by the sensor 1 and sensor 2, respectively. Then, the acceleration transmissibility can be calculated by Eq. (28) and the transmissibility vs. frequency curves were derived. For comparison, two transmissibility vs. frequency curves were plotted: one was obtained without tuning the resonant frequency of the RFTVI, and the other was under the condition that the resonant frequency of the RFTVI is tuned.
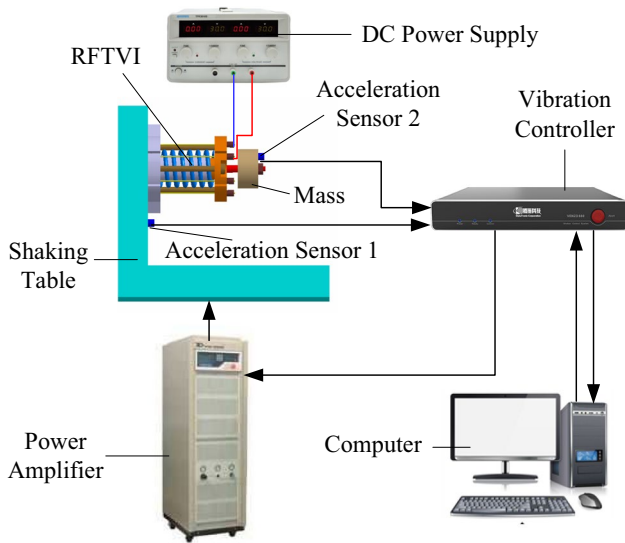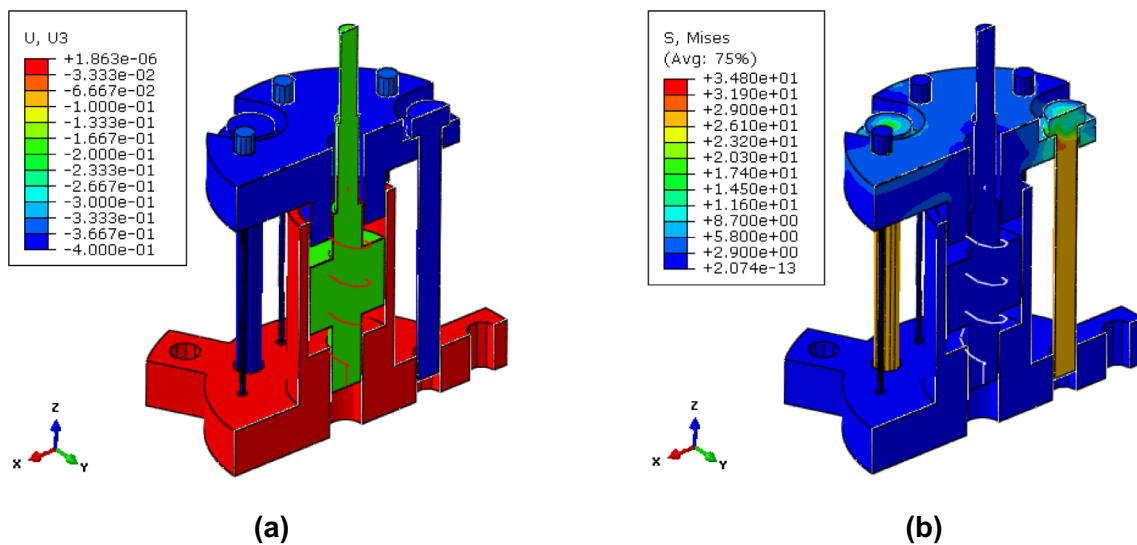

Fig. 15 Experimental platform

Fig. 16 Simulation results of **a** displacement in axis direction and **b** equivalent stress for the first load step

Results and Discussion

The First Load Step

Figure 16a, b shows the displacement in the axial direction and the equivalent stress distribution, respectively, for the first load step. It can be seen that the guide bolts contracted 0.4 mm in axial direction, and the upper plate produced a corresponding displacement of 0.4 mm. The maximum equivalent stress of 34.8 MPa is generated at the contact area between the guide bolts and the upper plate, which verifies that the tensile strength 980 MPa of the guide bolts meets the application requirements.

Based on the simulation results, a force–displacement curve of metal rubbers was plotted and compared with experimental results, as shown in Fig. 17. Since the force–displacement curves of the two metal rubbers are identical, this figure can represent the performance of either of the two metal rubbers. It can be seen that with the increase of force, the displacement increases gradually until it reaches the maximum value of 0.2 mm. In addition, we can see that the curve is in good agreement with the experimental results, which demonstrates that it is reasonable to use the TRANS-LATOR CONNECTOR elements to simplify metal rubbers. By calculating the tangent slope of each data point of the cure, we can obtain the tangent stiffness of metal rubber is 37 N/mm at the end of the first load step. If a 1 kg mass is installed on the top of the movable spindle, it can be calculated that the natural frequency of the RFTVI is 42.6 Hz.

The Second Load Step

Figure 18a–d shows the temperature, martensitic volume fraction, displacement in axis direction, and equivalent stress
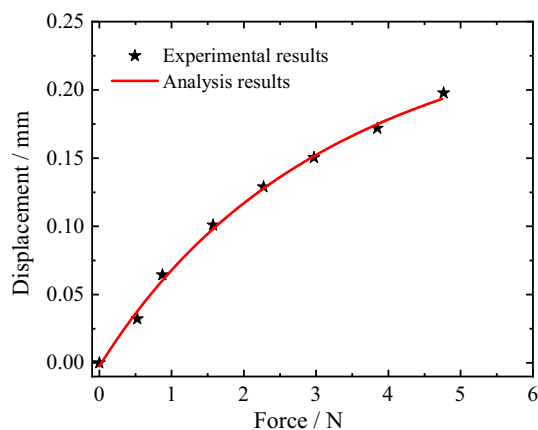

Fig. 17 Force vs. displacement curve of a metal rubber for the first load step

distribution, respectively, for the second load step. It can be seen from Fig. 18a that the temperature of the SMA wire is 400 K, while the temperatures of other components are maintained at 280 K.

The martensitic volume fraction distribution of SMA wires is shown in Fig. 18b. Because the temperatures of SMA wires rose from 280 to 400 K, the SMA wires transformed from martensite to austenite, which leads to the decrease in the martensitic volume fraction. As can be seen, the martensitic volume fraction is only 1.3×10^{-3} at 400 k. It can be said that the SMA wires are almost in a fully austenitic state.

In addition, we can see that the maximum displacement of the upper plate is 0.9 mm, of which the displacement of 0.5 mm is induced by the contraction of the SMA wires. Then, the total displacement of the upper plate is obtained by adding 0.5–0.4 mm of the first load step. After the second load step, due to the separation of the guide bolts and the upper plate, the elastic force of the spring acts on the SMA wires with the help of the upper plate. Furthermore, the equivalent tensile stress of the SMA wires is increased to 350 MPa, as shown in Fig. 18d.

Based on the simulation results, the strain vs. temperature and martensitic volume fraction vs. temperature curves are plotted, as shown in Fig. 19a, b, respectively. According to the variation of the slope of the curves, the two curves can be divided into five stages. In the first stage, the strain increases slowly with the increase of temperature, which is caused only by the thermal expansion of the SMA wires, as shown in Fig. 19a. In this process, the martensitic volume fraction remains unchanged, because the temperature is lower than A_s, as shown in Fig. 19b. When the temperature rises to 328 K, which is higher than A_s, the reverse transformation from martensite to austenite occurs, resulting in the contraction of SMA wires. Therefore, the strain and martensitic volume fraction decrease simultaneously until the temperature reaches 331 K. This process is the second stage. When the temperature is higher than 331 K, the contraction of SMA wires are restricted, because the fixers of SMA wires are blocked by the upper plate. Thus, the decreasing rates of strain and martensitic volume fraction slow down until the temperature rises to 374 K, which is called the third stage. When the temperature is higher than 374 K, the strain and martensitic volume fraction are decreased sharply until the temperature rises to 381 K, which is the fourth stage. This stage is formed by the separation of contact between guide bolts and the upper plate caused by the increasing of contraction force of SMA wires. When the temperature is 380 K, all martensite has transformed into austenite, that is, the martensitic volume fraction is zero. Thereafter, with the increase of temperature, the martensitic volume fraction
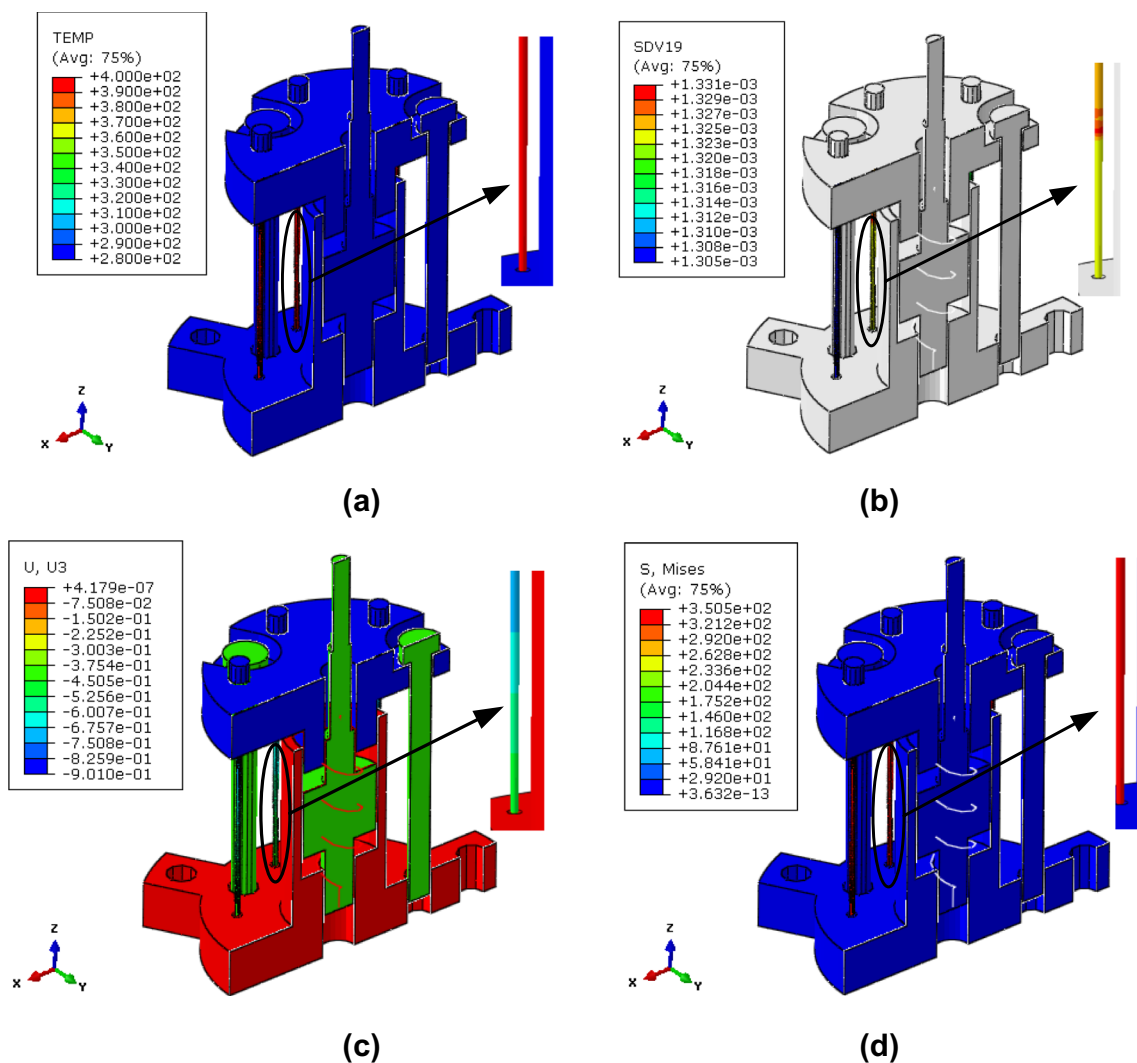
Fig. 18 Simulation results of **a** temperature, **b** martensitic volume fraction, **c** displacement in axis direction, and **d** equivalent stress for the second load step

remains zero (see Fig. 19b), while the strain of SMA wires increases gradually due to the influence of thermal expansion until the temperature rises to 400 K (see Fig. 19a). The last process is called the fifth stage.

The force vs. displacement curve of the metal rubbers for the second load step is plotted, as shown in Fig. 20, in which the corresponding experimental data are also depicted for comparison. It is observed that the displacement increases gradually with the increase of force until it reached the maximum value of 0.45 mm. The variation trend of displacement with force is consistent with the experimental data. By calculating the tangent slope of each point of the curve, it can

be obtained that the tangent stiffness of the metal rubber is 312 N/mm at the end of load step. If a 1 kg mass is installed on the top of the movable spindle, it can be calculated that the natural frequency of the RFTVI is 122.7 Hz, which is higher than the frequency 42.6 Hz at the end of the first load step.

Isolation Performance of the RFTVI

Figure 21 shows the acceleration transmissibility vs. frequency cures of the RFTVI under different states. The blue solid curve with circle points was obtained before the
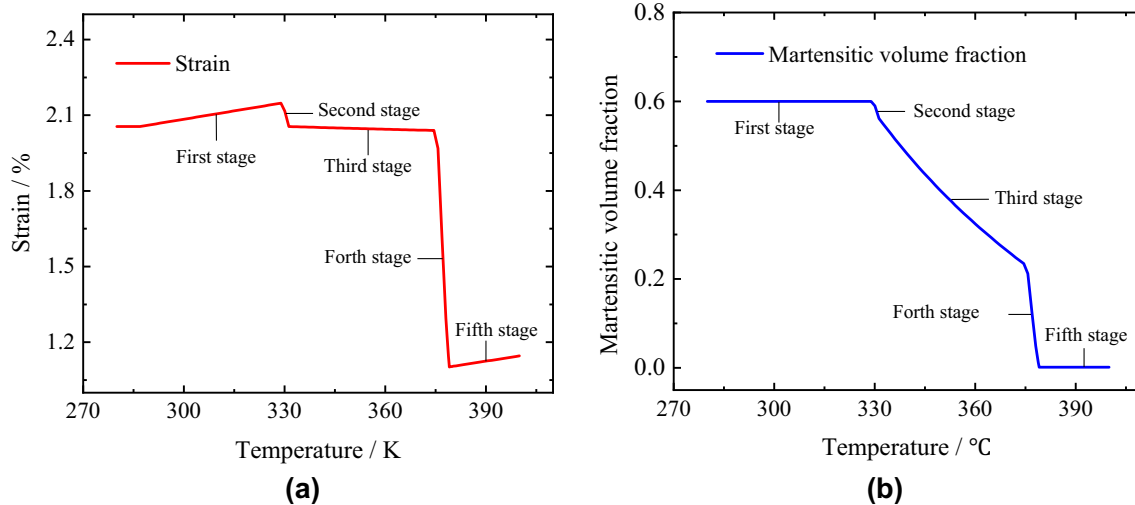
Fig. 19 Curves of **a** strain vs. temperature and **b** Martensitic volume fraction vs. temperature for the second load step
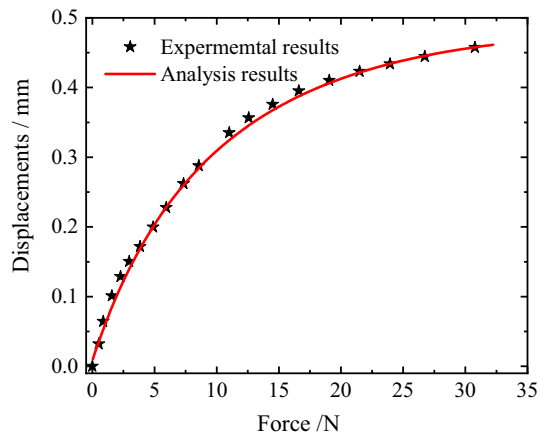

Fig. 20 Force vs. displacement curve of metal rubbers for the second load step

Fig. 21 Acceleration transmissibility vs. frequency curves of the RFTVI in two states

resonant frequency tuning, and the red solid cure with square points was after the resonant frequency tuning.

It can be seen from the figure that the resonant frequency before frequency tuning is 41 Hz, while the resonant frequency after frequency tuning is 121 Hz, which verifies that the resonant frequency of the RFTVI is tunable and the FEA of the RFTVI is feasible. The two resonant frequencies obtained from the test are lower than the analysis results of 42.6 and 122.7 Hz, respectively, because the stiffness of the RFTVI in the test is lower than that in the FEA. In addition, the peak value of the acceleration transmissibility after frequency tuning is great than that before frequency tuning, which is caused by the reduction of the damping of the RFTVI. When the resonant frequency is tuned, the metal rubbers in the RFTVI are compressed, so that the relative
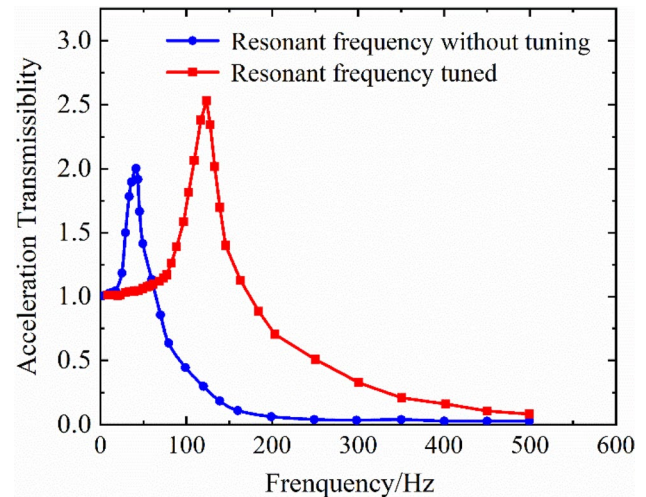
sliding among metal wires becomes more difficult. Thus, the efficiency of energy absorption through the sliding of metal wires decreases, resulting in the reduction of the damping of the RFTVI.

Summary and Conclusion

To simulate the mechanical behaviors of the RFTVI with SMA wires, the UMAT subroutine was programmed based on the unified SMA constitutive model and implemented in the ABAQUS environment. The validation of the UMAT subroutine was demonstrated by simulating the

pseudoelasticity of SMA wires. Then, a 3D model of the RFTVI was created. The TRANSLATOR CONNECTOR elements and corresponding nonlinear mechanical characteristics were adopted to simulate the mechanical behaviors of the two metal rubbers. The SPRING element and the corresponding mechanical characteristics were adopted to simulate the mechanical behavior of the spring. A martensitic volume fraction of 0.6 and an initial transformation strain of 0.02 of the SMA wires were initialized. Then, two-load steps were defined to simulate the mechanical behaviors of the tightening process of the guide bolts and the activation process of the SMA wires, respectively. The mechanical characteristics, such as displacements, equivalent stresses, temperatures, and martensitic volume fractions, are calculated, which reveal the mechanical behaviors of the RFTVI. Meanwhile, the isolation performance of the RFTVI was investigated and demonstrated.

For all of the above results, the following conclusions can be drawn. The UMAT subroutine, based on the unified SMA constitutive model, is valid for simulating the mechanical characteristics of the SMAs. The TRANSLATOR CONNECTOR elements and SPRING elements can be used to substitute the components of metal rubbers and springs, respectively. The two-load step procedure is suitable for simulating the mechanical behavior of the tightening process of the guide bolts and the activating process of the SMA wires. The results reveal the mechanical behaviors and isolation performance of the RFT vibration isolator. The simulation methods adopted in this paper are useful for designing RFTVIs.

Availability of Data and Materials The data used to support the findings of this study are included within the article.

Code Availability Not applicable.

Declarations

Conflicts of Interest The authors declare that there is no conflict of interest.

Ethics Approval Not applicable.

Consent to Participate Not applicable.

Consent for Publication Not applicable.

References

1. Chen J, Shen X, Tu F, Qureshi EM (2014) Experimental research on an active sting damper in a low speed acoustic wind tunnel. Shock Vib 2014:1–10
2. Johnson CD, Wilke PS, Pendleton SC (2006) Softride vibration and shock isolation systems that protect spacecraft from launch dynamic environments. In Proceedings of the 38th aerospace mechanisms symposium, Langley Research Center.
3. Li M, Cheng W, Xie R (2021) A quasi-zero-stiffness vibration isolator using a cam mechanism with user-defined profile. Int J Mech Sci 189:105938
4. Zhang F, Shao S, Tian Z, Xu M, Xie S (2019) Active-passive hybrid vibration isolation with magnetic negative stiffness isolator based on Maxwell normal stress. Mech Syst Signal Process 123:244–263
5. Liu C, Yu K, Tang J (2020) New insights into the damping characteristics of a typical quasi-zero-stiffness vibration isolator. Int J Non-Linear Mech 124:103511
6. Liu C, Yu K, Liao B, Hu R (2021) Enhanced vibration isolation performance of quasi-zero-stiffness isolator by introducing tunable nonlinear inerter. Commun Nonlinear Sci Numer Simul 95:105654
7. Chen Y, Wen H, Jin D (2020) Design and experiment of a non-contact electromagnetic vibration isolator with controllable stiffness. Acta Astronaut 168:130–137
8. Sun X, Jing X (2015) Multi-direction vibration isolation with quasi-zero stiffness by employing geometrical nonlinearity. Mech Syst Signal Process 62:149–163
9. Ye K, Ji J, Brown T (2021) A novel integrated quasi-zero stiffness vibration isolator for coupled translational and rotational vibrations. Mech Syst Signal Process 149:107340
10. Zhang Q, Xia S, Xu D, Peng Z (2020) A torsion–translational vibration isolator with quasi-zero stiffness. Nonlinear Dyn 99:1467–1488
11. Zhou J, Xiao Q, Xu D, Ouyang H, Li Y (2017) A novel quasi-zero-stiffness strut and its applications in six-degree-of-freedom vibration isolation platform. J Sound Vib 394:59–74
12. Xu J, Sun X (2015) A multi-directional vibration isolator based on Quasi-Zero-Stiffness structure and time-delayed active control. Int J Mech Sci 100:126–135
13. Melentjev VS, Gvozdev AS, Bezborodov SA (2017) Investigation of the ring vibration isolator, the characteristics of which are regulated by changing the radius of curvature and angle of coverage. Procedia Eng 176:567–576
14. Zhao Y, Meng G (2020) A bio-inspired semi-active vibration isolator with variable-stiffness dielectric elastomer: design and modeling. J Sound Vib 485:115592

15. Yan B, Ma H, Zhao C, Wu C, Wang K, Wang P (2018) A vari-stiffness nonlinear isolator with magnetic effects: theoretical modeling and experimental verification. Int J Mech Sci 148:745–755

16. Yan B, Ma H, Zhang L, Zheng W, Wang K, Wu C (2020) A bistable vibration isolator with nonlinear electromagnetic shunt damping. Mech Syst Signal Process 136:106504

17. Wu T-H, Lan C-C (2016) A wide-range variable stiffness mechanism for semi-active vibration systems. J Sound Vib 363:18–32

18. Le TD, Nguyen VAD (2017) Low frequency vibration isolator with adjustable configurative parameter. Int J Mech Sci 134:224–233

19. Rahman M, Ong ZC, Julai S, Ferdaus MM, Ahamed R (2017) A review of advances in magnetorheological dampers: their design optimization and applications. J Zhejiang Univ Sci A 18:991–1010

20. Yang J, Ning D, Sun S, Zheng J, Lu H, Nakano M, Zhang S, Du H, Li W (2021) A semi-active suspension using a magnetorheological damper with nonlinear negative-stiffness component. Mech Syst Signal Process 147:107071

21. Hashi HA, Muthalif AG, Nordin ND (2016) Dynamic tuning of torsional transmissibility using magnetorheological elastomer: modelling and experimental verification. Iran J Sci Technol Trans Mech Eng 40:181–187

22. Jose S, Chakraborty G, Bhattacharyya R (2017) Coupled thermomechanical analysis of a vibration isolator made of shape memory alloy. Int J Solids Struct 115:87–103

23. Shen X, Chen Y, Wang J, Li J, Chang L, Sun Y (2019) Design, experiment and verification of resonant frequency-tunable vibration isolator based on annular metal rubbers and shape memory alloy actuators. J Vib Eng Technol 7:277–289

24. Qidwai M, Lagoudas D (2000) Numerical implementation of a shape memory alloy thermomechanical constitutive model using return mapping algorithms. Int J Numer Meth Eng 47:1123–1168

25. Roh J-H, Han J-H, Lee I (2006) Nonlinear finite element simulation of shape adaptive structures with SMA strip actuator. J Intell Mater Syst Struct 17:1007–1022

26. Lagoudas DC (2008) Shape memory alloys: modeling and engineering applications. Springer, New York

Publisher's Note Springer Nature remains neutral with regard to jurisdictional claims in published maps and institutional affiliations.